ADVANCED OPTICAL MATERIALS
www.advopticalmat.de

Quasi-BIC Enhanced Broadband Terahertz Generation in All-Dielectric Metasurface

Leyong Hu, Bo Wang, Yang Guo, Shuo Du, Jianing Chen,* Junjie Li, Changzhi Gu,* and Li Wang*

Terahertz waves have widespread applications in various fields ranging from wireless communication to fundamental physics. Achieving bright and broadband terahertz sources still remains a challenge. Recent research has revealed that all-dielectric metasurfaces with strong electromagnetic resonances and negligible Ohmic loss can enhance nonlinear optical processes and weaken the influences of phase-matching conditions, providing new opportunities for developing terahertz sources. Here, an all-dielectric metasurface supporting quasi-BIC (bound states in the continuum), which enhances terahertz emission in a nonlinear optical film under the excitation of femtosecond laser pulses, is proposed. It is observed that the terahertz emission in lithium niobate ($LiNbO_3$) films is enhanced up to 17 times by a silicon dioxide metasurface and that the terahertz emission enhancement spans the frequency range in 0.1–4.5 THz. This mechanism for the terahertz emission enhancement is attributed to the tight confinement of the pump field in the $LNibO_3$ which is caused by quasi-BIC resonances. The all-dielectric metasurface is patterned on the $LiNbO_3$ film instead of etching it, providing a simple way for engineering nonlinear optical processes in $LiNbO_3$. This work paves the way for broadband terahertz emitters.

1. Introduction

Terahertz science and technology have broad application prospects in various fields such as spectroscopy, wireless communication, security imaging, and sensing.[1–8] Since the fundamental resonances of many materials lie in the frequency range of 0.1–10 THz,[2,7] efficient broadband terahertz emitters are highly desirable to facilitate the applications of terahertz waves. Most broadband desktop terahertz sources are driven by ultrashort laser pulses via optical rectification (OR),[9–11] a second-order nonlinear optical effect. However, this effect requires rigorous phase-matching conditions[12] to achieve bright terahertz sources, which limits the choices of nonlinear materials and laser wavelength. OR thin-film materials such as lithium niobate (LN) are promising candidates to overcome these limitations, as the effect of phase-matching conditions is greatly attenuated by the shorter propagation length.[13–15] However, bare OR thin films are inefficient in radiating terahertz waves due to the short effective generation length.[12,16] Therefore, it is crucial to improve the terahertz emission efficiency of OR thin films.

Previous studies suggest that metasurfaces can enhance nonlinear optical processes, creating numerous applications in photonics.[17–24] In particular, nonlinear plasmonic metasurfaces have been demonstrated to emit broadband terahertz waves[25–29] due to their local field enhancement[30] and resonant nonlinearity.[31] However, plasmonic nanostructures exhibit considerable ohmic loss, low damage threshold, and small volumes,[17] which would remarkably hinder nonlinear conversion efficiency. In contrast, all-dielectric metasurfaces address the critical issue of heat dissipation. Furthermore, all-dielectric metasurfaces have already shined in various nonlinear processes benefitting from the significant nonlinear coefficients and have great potential in developing efficient terahertz emitters. In fact, silicon surface nanostructures have been demonstrated to emit terahertz waves due to the symmetry breakings,[44,45] but both the efficiency and bandwidth require to be improved.

Bound states in the continuum (BICs) that are identified as localized states coexisting with extended modes within light cones, have already been realized in various systems[32,33] such as photonic crystals, metasurfaces, and waveguides. The BIC concept is helpful to design extremely sharp resonators for enhancing light-matter interactions at the subwavelength scale. For example, they have already been applied in lasing,[34]sen sing,[35] harmonic generations.[36] Furthermore, it recently has been demonstrated[37,38] that patterning a low-refractive-index

L. Hu, B. Wang, Y. Guo, S. Du, J. Chen, J. Li, C. Gu, L. Wang
Beijing National Laboratory for Condensed Matter Physics
Institute of Physics
Chinese Academy of Sciences
Beijing 100190, P. R. China
E-mail: wangbo2014@iphy.ac.cn; jnchen@iphy.ac.cn; czgu@iphy.ac.cn
L. Hu, Y. Guo, S. Du, J. Li, C. Gu
School of Physical Sciences
CAS Key Laboratory of Vacuum Physics
University of Chinese Academy of Sciences
Beijing 100190, P. R. China
B. Wang
Wenzhou Institute
University of Chinese Academy of Sciences
Wenzhou, Zhejiang 325001, P. R. China
J. Li
Songshan Lake Materials Laboratory
Dongguan, Guangdong 523808, P. R. China
The ORCID identification number(s) for the author(s) of this article can be found under https://doi.org/10.1002/adom.202200193.

DOI: 10.1002/adom.202200193

material on an LN substrate is able to produce a BIC, which can confine and guide light in the region of LN. Due to the large linear and nonlinear susceptibility of LN, a BIC supported by the LN capped with a low-refractive-index photonic structure can enhance the nonlinear optical processes,[37,38] which brings new opportunities for ultrathin broadband terahertz emitters.

This paper demonstrates an efficient terahertz source based on an all-dielectric metasurface that enables up to 17 times enhancement of terahertz electric fields across a broad spectral range. The metasurface is composed of patterned a silicon dioxide (SiO_2) layer and an LN film, supporting quasi-BIC induced by breaking the mirror and rotational symmetry. The coupling between a magnetic-dipole mode and an electric-dipole one localizes the pump fields into the high-refractive-index LN film, and thus avoids the complicated process of LN etching. As a result, the terahertz generation from LN is strikingly enhanced. Our work not only breaks the new ground for developing efficient broadband terahertz sources but also expands the application of all-dielectric metasurfaces.

2. Results

2.1. Working Principle and Metasurface Design

We first explain the working principle for our all-dielectric metasurfaces. **Figure 1**a shows the schematic of enhancing terahertz generation by the all-dielectric metasurfaces under the excitation of the near-infrared (NIR) femtosecond laser pulses. The sample consists of an x-cut LN film on an insulating substrate

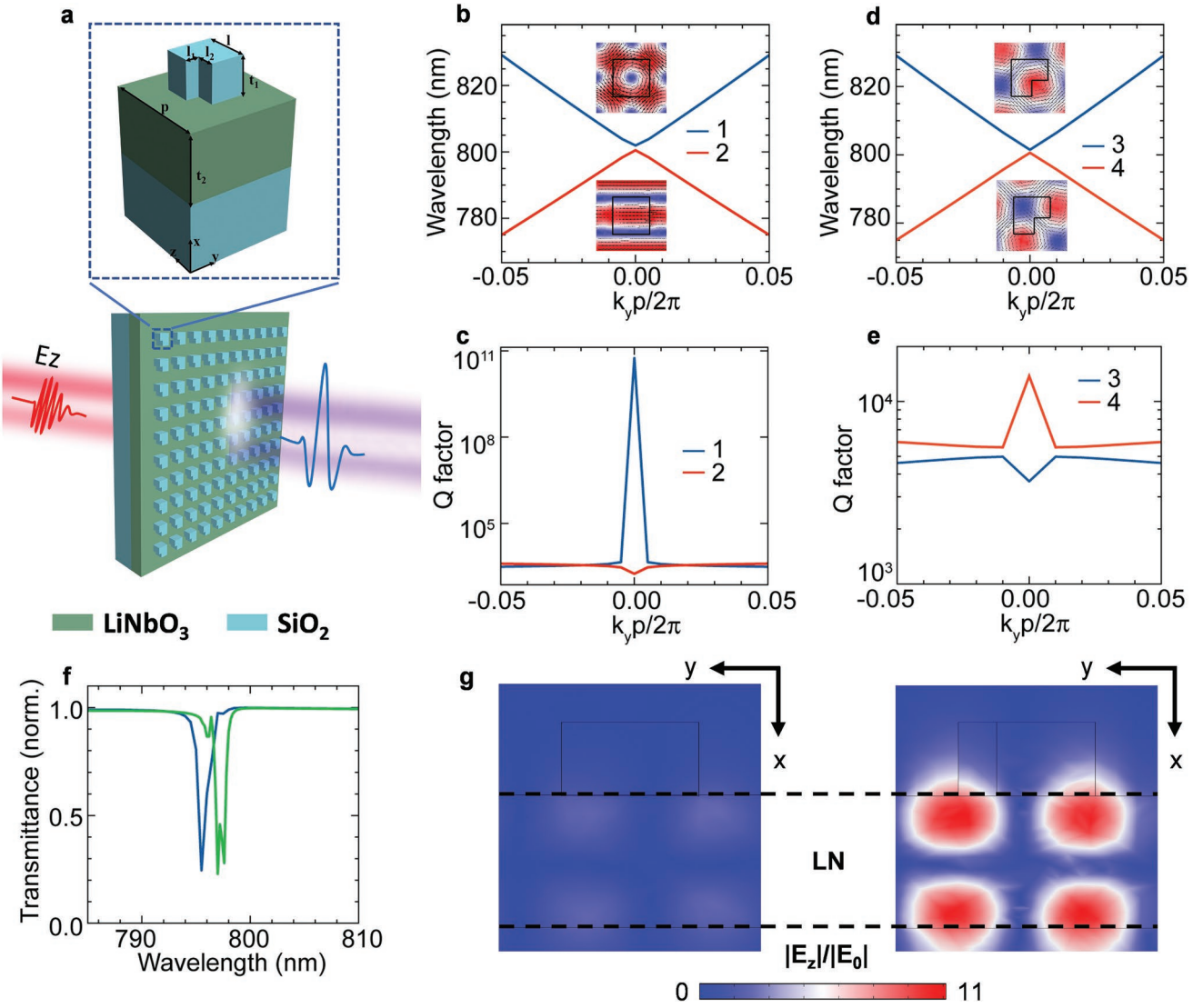

Figure 1. Work principle and BIC. a) Artists view of terahertz emission enhancement by all-dielectric metasurface: the pump laser pulses and the emitted terahertz waves polarized along the optical axis (z-axis) of an x-cut LN. The parameter for the L-shaped metasurface (LMS) are: $p = 480$ nm, $t_2 = 360$ nm, $t_1 = 200$ nm, $l = 250$ nm, $l_1 = 70$ nm, $l_2 = 110$ nm. The LMS results from adding an in-plane defect on a square-shaped metasurfaces (SMS). b The band diagrams and c) Q factor of the SMS. d) Band diagram and e) Q factor of the LMS. f) Calculated linear transmission spectra of SMS and LMS. g) The electric field distributions (x–y cross section) at the resonances of SMS (left) and LMS (right).

(LNOI) capped a SiO_2 metasurface. We choose the *x*-cut LNOI to ensure that the orientation with the largest nonlinear coefficient (d_{33}) is in-plane. The electric field of the pump light polarizes along the optic axis of LN (*z*-axis). As the metasurface building block, we select an L-shaped nanoresonator, formed by an in-plane perturbation on an $l \times l$ square (l = 250 nm) nanoresonator. An array of meta-atoms are arranged in a square lattice with the array pitch of p = 480 nm. Our dielectric metasurface supports high-Q factor resonances responsible for confining the pump fields inside the LN film.

To reveal the mechanism of the field enhancement in LN, we calculated the electromagnetic eigenmodes of the unperturbed square nanoresonators; see the Experimental Section for details. The square metasurface (SMS) supports a BIC (Mode 1) with an infinite Q factor at the point of the first Brillouin zone (see Figure 1b and Figure 1c). The electric field distribution of Mode 1 (see the inset of Figure 1b) presents a magnetic dipole nature polarizing along the *x*-axis (M_x). The BIC mode is prohibited from coupling with external electromagnetic waves and thus does not contribute to the enhancement of terahertz emission. An electric-dipole mode (mode 2) exists near the BIC mode, polarizing along the *z*-axis (P_z) with a finite Q factor (1758) (see Figure 1b,c). The electric dipole mode nearly cannot boost the terahertz generation due to symmetry constraints, though it can slightly confine the pump fields inside the LN film (see the left plane of Figure 1g); see Note S3 (Supporting Information) for the symmetry analysis.

Due to the existence of a mirror plane in the *x*–*z* plane (σ_{xz}), the M_x of mode 1 is independent of the P_z of mode 2; see the detailed analysis in Note S2 (Supporting Information). Once the spatial symmetry is broken or k_y increases, the two modes are inter-coupled. We employ an effective 2 × 2 Hamiltonian to illustrate the coupling of the two modes

$$H = \begin{bmatrix} \omega_1 & U \\ V & \omega_2 + \gamma_2 i \end{bmatrix} \tag{1}$$

where ω_1 and ω_2 are the eigenfrequencies of the two uncoupled modes. Here, $\omega_1 \approx \omega_2$, γ_2 denotes the damping rate of mode 2, UV is the coupling strength. The eigenfrequencies of the two mixed modes are then written as

$$\omega_{\pm} = \omega_1 + \frac{\gamma_2}{2} i \pm \sqrt{UV - \frac{\gamma_2^2}{4}} \tag{2}$$

Since the U and V usually are complex due to the non-Hermiticity of the system, the real and imaginary parts of $\omega_{\pm}$ vary with the coupling strength. As presented in Figure 1b,c, the resonant wavelength of Mode 1 is redshifted, and its Q factor decreases from infinity to finite values as k_y departs from 0. In this case, the BIC mode becomes a quasi-BIC mode. Mode 2 presents an inverse trend.

The L-shaped metasurface (LMS) breaks the mirror symmetry, resulting in the coupling between M_x and P_z. We calculated the eigenmode of the LMS, as shown in Figures 1d,e. Two hybrid modes (Modes 3 and 4) are formed with both magnetic and electric dipole features; see the inset of Figure 1d. Mode 3 has a finite Q factor of 13 768 at the Γ point of the Brillouin zone, indicating that it is a quasi-BIC. The Q factor of the quasi-BIC approximately scales as an inverse square law with the asymmetry degree of the LMS (see Figure S3, Supporting Information), which is consistent with the previous report.[46] The quasi-BIC confines and enhances the optical electric fields inside the LN, as shown in the right plane of Figure 1g. The enhanced optical electric field can enhance terahertz nonlinear polarization in LN, which is the dominant mechanism for enhancing terahertz generation.

2.2. Sample Characterization and Terahertz Generation

We fabricated the SiO_2 metasurface (SMS and LMS) on the LNOI by electron-beam lithography (EBL) technique; see the Experimental Section and Figure S1 (Supporting Information) for detailed fabrication procedures. The dimension spans 2 mm × 2 mm, and the SEM images (See **Figure 2**a,b) confirm the high quality of our fabrication. We measured the transmittance of the SMS and LMS (see the Experimental Section for detailed information), as shown in Figure 2c. For the SMS, the transmission spectrum presents a resonant dip at 800 nm, which results from the electric-dipole mode. The Q factor of this resonant mode is 344, which is extracted from a rational fitting (red line of Figure 2c) on the transmission spectrum, see Note S5 (Supporting Information) for detailed procedures. The BIC exhibits no resonant structure in the transmittance spectra. For the LMS, a split dip is observed in the transmittance spectra, indicating that it is quasi-BIC. The two resonant modes have *Q*-factors of 201 and 453. The measured resonances are broader and slightly red-shifted compared with the calculated spectra (see Figure 1f). The deviations between the experiments and simulations may result from the fabrication imperfections such as the inclination of the meta-atom walls which is difficult to be included in the simulations. In addition, the incident light was focused onto the samples in experiments while a plane-wave source was used in the simulations.

We illuminated our samples (LN, LN+SMS, and LN+LMS) with NIR laser pulses (central wavelength 800 nm, repetition rate 80 MHz, duration 70 fs) and measured the terahertz generation by our homemade terahertz time-domain spectroscopy; for a detailed description of the experimental setup, see the Experimental Section and Figure S2 (Supporting Information). The terahertz time-domain electric fields polarizing along the *z*-axis from the three samples were measured under identical pumping and probe circumstances. The measured terahertz waveforms are shown in Figure 2d. One can see that, compared with the terahertz signal from LN, SMS has little influence on the terahertz generation; in contrast, LMS considerably increases the terahertz signal. The peak value of the LN+LMS pulse is about 8 times larger than that of the LN pulse. These results confirm the critical role of symmetry breaking and quasi-BIC in enhancing terahertz emission.

As seen in Figure 2d, the peak position of the LN+LMS pulse is shifted compared with that of the LN pulse, revealing that the enhancement is dispersive in the terahertz range. We perform the Fourier transform of the terahertz pulses to investigate the enhancement further. As seen in Figure 2e, the enhancement of the terahertz amplitude spans the entire

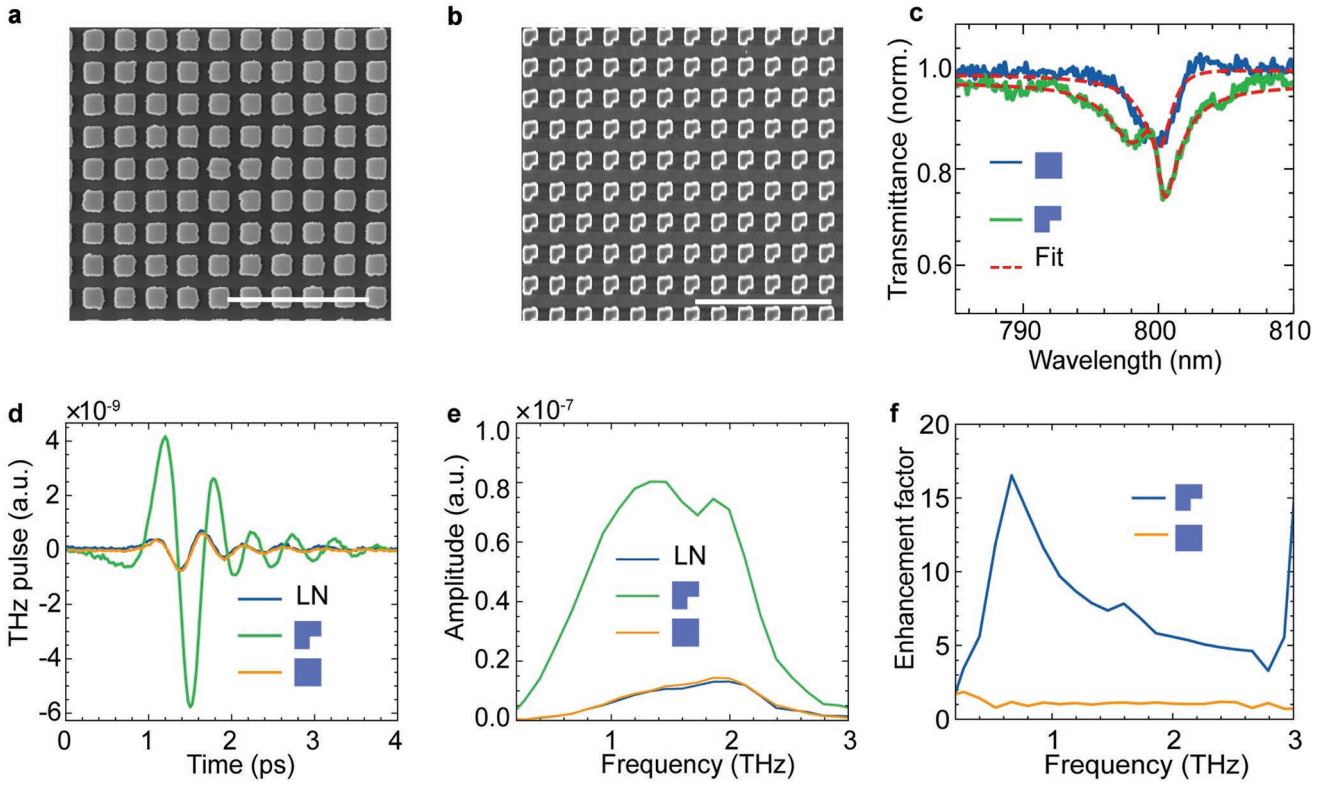

Figure 2. Sample characterization and terahertz emission. Scanning electron microscope (SEM) image of the fabricated metasurfaces showing an array of a) square-shaped and b) L-shaped nanostructures. Scale bars: 2 µm. The dimension of our metasurface is 2 mm × 2 mm. c) Experimental linear transmission spectra of SMS and LMS. SMS: square-shaped metasurface; LMS: L-shaped metasurface. The red lines denote fitting results by a rational model. d) The measured terahertz waveforms from the bare LN film, LMS, and SMS and e) their Fourier transform spectra. f) The enhancement factor of LMS and SMS, defined by the terahertz amplitudes ratio between the metasurface samples and LN film.

operating bandwidth of the detector (0.1–3 THz), but the detection frequency range is restricted by the thickness of ZnTe (2 mm). Utilizing a thinner ZnTe crystal (300 µm) as a detector, the detected enhanced bandwidth of the terahertz emission approaches 4.5 THz, as shown in Figure S6 (Supporting Information). The enhancement factor, terahertz amplitudes divided by the terahertz amplitude of LN, reaches 17 around 0.7 THz for the LMS+LN sample, as shown in Figure 2f. Inversely, the enhancement factor for the SMS+LN sample almost maintains 1 in the entire bandwidth of the detection. All of these findings show that our BIC-based all-dielectric metasurface can efficiently boost terahertz emission in the broadband range.

To further understand the enhancement of the terahertz emission by LMS, we calculated the field enhancement of pump light inside the LN region, as shown in Note S4 and Figure S4a (Supporting Information). Although the calculated enhancement factor reaches as high as 37 at 795 nm, the average enhancement factor is ≈3.14 in the spectral region between 790 and 810 nm where the pump laser pulses cover. According to the nonlinear optical theory, the average enhancement factor of terahertz emission is ≈10, which is in the same order as the experimental results. Additionally, we perform FDTD simulation to simulate terahertz generation from the LMS sample, as shown in Figure S5 and Note S6 (Supporting Information). The terahertz enhancement occurs in 0.1–3.5 THz, which is narrower than the experiment results. The maximum enhancement factor is 17.8 at 0.13 THz. The deviation between the experiment and simulation may come from the experimental *Q*-factor of the resonant modes far smaller than the simulated ones.

2.3. The Properties of Terahertz Generation from LN+LMS

To further characterize the terahertz emission of LN+LMS, we determined the dependence of the terahertz signal on the pump power. Since varying the pump power changes the amplitude without modifying the shape of terahertz pulses, we add the terahertz amplitudes from 0.1 to 3 THz and plot the sum amplitude changing with pump power, as shown in **Figure 3**a. The linear dependence is evident, indicating a second-order nonlinear process. In addition, we examine the dependence of the terahertz signal on the pump polarization. The results are shown in Figure 3b. The experiment data are perfectly fitted by a function $a\cos^2(\theta) + b\sin^2(\theta)$, ($a$ and b are fitting constants). This relation is determined by the $3m$ point group of LN (see Note S1, Supporting Information), which indicates that the symmetry breaking of the metasurfaces has little influence on the polarization dependence of the terahertz emission.

To determine the resonant characteristics of the terahertz emission enhancement, we altered the pump wavelength and measured the terahertz emission from LN capped with an LMS

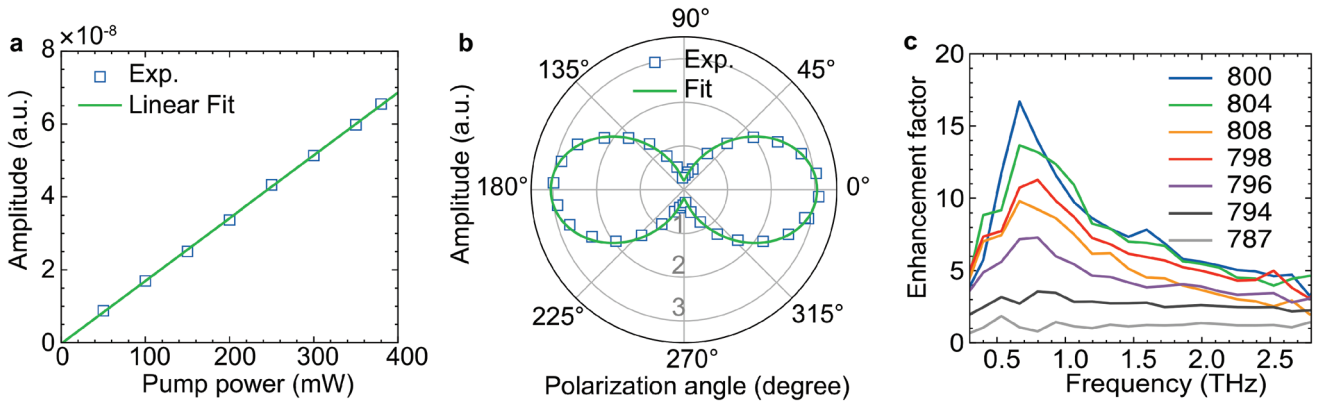

Figure 3. The properties of the terahertz generation from LN+LMS. a) Dependence of the terahertz amplitude on the pump power (blue square) and a linear fit (green line). b) Dependence of the terahertz electric fields on the pump polarization. The blue squares denote the experimental data and the green line represents fit results by the function $a\cos^2\theta + b\sin^2\theta$, where θ is the polarization angle, a and b are parameters. (c) The spectra of enhancement factor varying with pump wavelength from 787 to 808 nm.

and from naked LN sheets. In Figure 3c, we depict the enhancement factors for different pump wavelengths. One can see that the enhancement factor decreases sensitively as the pump wavelength deviates from 800 nm. When the pump wavelength is tuned to 787 nm, the enhancement nearly vanishes. These results confirm the resonant enhancement of terahertz generation by the quasi-BIC modes.

2.4. Incident Angle Dependence of Terahertz Generation from LN+LMS

The incident angle dependence of terahertz generation from LN+LMS is illustrated in **Figure 4**, which provides a unique angle on the relation between the terahertz emission enhancement and quasi-BIC. The terahertz pulses and spectra excited

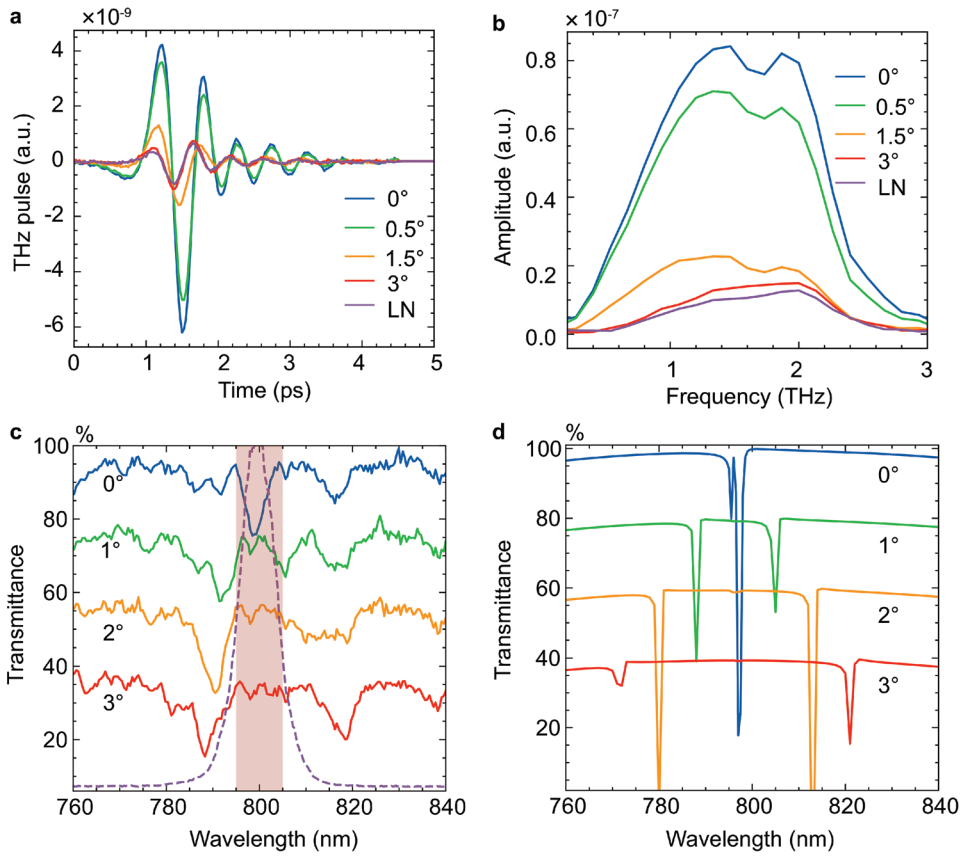

Figure 4. The dependence of terahertz generation from LN+LMS on the incident angle of pump beam. a) The generated terahertz waveforms and b) the corresponding spectra under the incident angles of 0°,0.5°,1.5°, and 3°. c) The measured and d) simulated evolution of transmission spectra versus incident angle from 0° to 3°. The dashed line represents the intensity profile of the laser pulses.

by pump light at different incident angles are shown in Figure 4a,b, respectively. It can be seen that the terahertz signal of LN+LMS achieves the largest value when the pump pulse is normally incident, and exhibits an immediate drop when the pump light is oblique; when the incident angle is greater than 3 degrees, the terahertz emission enhancement nearly disappears. This sensitive dependence of terahertz signals on the incident angle can be understood through the strong coupling between the in-plane electric-dipole mode (P_z) and out-plane magnetic-dipole mode (M_x). As the incident angle increases, the coupling strength (UV) between P_z and M_x is enhanced and the eigenfrequencies of the two modes mutually repel, which is evidenced by the transmittance spectrum. The experimental (Figure 4c) and simulated (Figure 4d) transmittance reveal two split dips; their separation increases with incidence angle. The resonant mode shifts weaken the local electric fields inside the LN film because the wavelength of the pump pulse remains unchanged, which explains our observations.

3. Discussion

It is helpful to make a brief comparison with other ultrathin terahertz emitters. The plasmonic SRRs have been demonstrated by Luo et al. [28] to emit terahertz waves about four times smaller than that from a 0.2 mm thick ZnTe crystal. However, the pump wavelength they used is 1500 nm, which largely deviates from the perfect phase-matching condition of ZnTe. In our case, the pump wavelength is 800 nm, where the ZnTe emits terahertz most efficiently. The generated terahertz signal from LN+LMS is about three times smaller than that from a 300 μm thick ZnTe crystal under the same condition (see Figure S7, Supporting Information), which is considered to be more efficient than plasmonic SRR emitter. As expected from the thin terahertz emitter, the terahertz signal from LN+LMS has a broader bandwidth than that from 1 mm thick ZnTe. Moreover, it seems that almost all reported plasmonic SRR terahertz emitters work near the pump wavelength of 1500 nm [25,26,28,39] to get rid of the strong loss at a shorter wavelength, which limits the pump wavelength for effective terahertz generation. For the LN+LMS emitter, there is little limitation on the pump wavelength as long as the resonant wavelengths are matched. Additionally, compared with ultrathin terahertz spin emitters, the LN+LMS emitters require no external magnetic fields. Finally, we should mention that the terahertz signal from LN+LMS is large enough to be applied in the TDS; see Note S7 and Figure S8 (Supporting Information) for our measurements on lactose powder.

LN is one of the most important crystals in nonlinear optics because of its large linear and nonlinear susceptibility. It is promising to combine metasurfaces with LN to engineer the linear and nonlinear optical processes. However, LN is difficult to etch. Available etching methods such as argon milling and plasma etching face the challenge of achieving steep sidewalls and large etching depths. [40] In addition, rough etched edges tend to introduce non-negligible losses. [41] Our experiment demonstrates that constructing metasurfaces on the LN film is an effective method to manipulate nonlinear processes, further releasing the potential of LNOI in nonlinear micro-nano photonics.

In this work, quasi-BIC modes are used to localize pump electric fields. Other resonant modes of the all-dielectric metasurface whose Q factors are adjustable, such as optical anapole [42] and surface lattice resonances, [43] may be also used in enhancing terahertz generation. In addition, we show in Note S4 and Figure S4 (Supporting Information) that the enhancement of the pump field caused by LMS is closely related to the asymmetry degree and there is a critical asymmetry degree for the highest enhancement factor. Therefore, our scheme for an effective ultrathin terahertz emitter can be further optimized.

4. Conclusions

In summary, we have designed and realized an all-dielectric metasurface on LNOI platforms to enhance broadband terahertz generation from LN film. An up to 17 times enhancement of terahertz amplitudes has been achieved. The mechanism for enhancing terahertz generation is ascribed to the quasi-BIC induced by symmetry breaking, which strongly confines the pump electric fields in the LN films. The all-dielectric metasurface-based terahertz emitter features broadband, high efficiency, and small dimension, which paves the way for highly compact terahertz systems.

5. Experimental Section

Sample Fabrication: The flow diagram of the sample fabrication is shown in Figure S1 (Supporting Information). The commercially available X-cut Lithium niobate on insulator (LNOI) wafers obtained from NANOLN, with a 360 nm thick LN layer bonded on top of a 2 μm thick silica buffer layer, were used for device fabrication. A 200 nm thick layer of silica was deposited using the Inductive Coupled Plasma deposition system (ICP-PECVD, SENTECH, SI500). The PMMA resister (200 nm) was spun on the wafers and patterned with electron-beam lithography (EBL, JEOL,6300FS). Then a 40 nm Al layer was deposited on the resister by a sequence with electron beam evaporation deposition (EBD) method. Then the Al film was stripped by removing PMMA, leaving the metal pattern on the substrate. Afterward, by using reactive ion etching (RIE, Oxford, NGP80), the desired structure was transferred from Al to silica. Finally, the Al mask was removed using Al etchant.

Numerical Calculations: The numerical simulations were mainly performed by using finite-difference time-domain (FDTD). The periodic boundary condition and perfectly matched layer were employed for the horizontal (x- and y-) and vertical (z-) directions in the simulation, respectively. The dielectric constants (ε) for simulations were imported from the experimental ellipsometry data. For Silica, $\varepsilon = 2.16$. For LN layers, ε along the ordinary and extraordinary axis were 6.57 and 4.73, respectively. In the simulations, the transmission spectrum, eigenmodes, electric field distributions, and other the electromagnetic properties of the metasurface were studied in detail.

Linear Transmittance Measurements of the Metasurfaces: The transmission spectra of the metasurface were measured with the home-built spectroscopy system. Near-infrared light was emitted from a stabilized tungsten light source. The incident beam was first focused onto the sample by a lens (focal length 10 cm). Then, the transmitted light was collected and collimated to a spectrometer (Idea Optics, PG400). The transmittance spectra were obtained by normalizing the measured spectrum of the metasurface to that of an unpatented reference area on the same substrate.

Terahertz Emission Spectroscopy: The experimental setup for terahertz emission is shown in Figure S2 (Supporting Information). A commercial

titanium- sapphire oscillator laser (Spectra-physics), delivering pulses of 70 fs with 800 nm central wavelength and 80 MHz repletion rate, was used as the laser source. The pulse was split by a beam splitter(12:1) into a pump beam and a probe beam. A half-wave plate was used to rotate the polarization plane of the pump beam. A mechanical chopper, synchronized with the lock-in amplifier, chopped the pump beam at 2220 Hz. The pump beam illuminated the samples with a typical average power of 380 mW (after chopper) and a 200 μm beam diameter (behind a lens with a focal length of 15 cm). The pump beam was normally incident on the sample surface, which the reflection light spot can check. After passing through the sample, the pump beam was blocked by a silicon mirror. The terahertz waves generated from the sample were collected and guided by four off-axis parabolic mirrors and then focused onto a 2 mm ZnTe crystal used as a terahertz detector. A metal wire-grid terahertz polarizer was used in the terahertz light path to ensure vertically polarized terahertz is detected. The probe beam passed through the ZnTe crystal, the refractive index of which was changed by the terahertz electric fields, with a change of polarization state. This change was proportional to the terahertz fields and detected by an instrument consisting of a quarter wave plate, a Wollaston prism, and a balanced detector. A lock-in amplifier amplified the balanced signal. The light path of the terahertz wave was sealed in a vacuum chamber to avoid the absorption of vapors.

Supporting Information

Supporting Information is available from the Wiley Online Library or from the author.

Acknowledgements

The authors acknowledge the supports from P. X. Li and Y. P. Yang for linear optical measurement, and from M. Z. Lv for language polishing. This work was supported by the National Natural Science Foundation of China under Grant Nos. 61888102, 11974386, 62174179, 12074420, U21A20140 and 61905274, the National Key Research and Development Program of China under Grant No. 2021YFA1400700, the Beijing Municipal Science & Technology Commission, Administrative Commission of Zhongguancun Science Park under Grant No. Z211100004821009, the Strategic Priority Research Program of Chinese Academy of Sciences (CAS) under Grant Nos. XDB33000000 and XDB28000000, the Key Research Program of Frontier Sciences of CAS under Grant Nos. QYZDJ-SSWSLH042 and XDPB22. and the Project for Young Scientists in Basic Research of CAS under Grant No.YSBR021. This work is also supported by the Synergic Extreme Condition User Facility, China.

Conflict of Interest

The authors declare no conflict of interest.

Author Contributions

L.H. and B.W. contributed equally to this work. B.W., J.C., and C.G. conceived the basic idea for this work. L.H. and S.D. fabricated the samples and conducted numerical simulations. B.W. conducted the terahertz emission experiments and gave the theoretical explanations. L.H., B.W. and Y.G. performed the optical measurement. J.C. and C.G supervised the research and the development of the manuscript. L.H and B.W. wrote the draft of the manuscript, and L.W. and J.L. took part in the discussion and revision. All authors approved the final copy of the manuscript.

Data Availability Statement

The data that support the findings of this study are available from the corresponding author upon reasonable request.

Keywords

all-dielectric, bound states in the continuum, metasurfaces, terahertz

Received: January 26, 2022
Revised: February 28, 2022
Published online:

[1] B. Ferguson, Xi-C Zhang, *Nat. Mater.* **2002**, *1*, 26.
[2] R. Ulbricht, E. Hendry, J. Shan, T F. Heinz, M. Bonn, *Rev. Mod. Phys.* **2011**, *83*, 543.
[3] M. Tonouchi, *Nat. Photonics* **2007**, *1*, 97.
[4] J. Federici, L. Moeller, *J. Appl. Phys.* **2010**, *107*, 111101.
[5] J. F. Federici, B. Schulkin, F. Huang, D. Gary, R. Barat, F. Oliveira, D. Zimdars, *Semicond. Sci. Technol.* **2005**, *20*, S266.
[6] T. Li, A. Patz, L. Mouchliadis, J. Yan, T A. Lograsso, I E. Perakis, J. Wang, *Nature* **2013**, *496*, 69.
[7] T. Kampfrath, K. Tanaka, K A. Nelson, *Nat. Photonics* **2013**, *7*, 680.
[8] S. Baierl, M. Hohenleutner, T. Kampfrath, A. K. Zvezdin, A. V. Kimel, R. Huber, R. V. Mikhaylovskiy, *Nat. Photonics* **2016**, *10*, 715.
[9] K. Reimann, *Rep. Prog. Phys.* **2007**, *70*, 1597.
[10] F. Blanchard, G. Sharma, L. Razzari, X. Ropagnol, H.- C. Bandulet, F. Vidal, R. Morandotti, J.- C. Kieffer, T. Ozaki, H. Tiedje, H. Haugen, M. Reid, F. Hegmann, *IEEE J. Sel. Top. Quantum Electron.* **2010**, *17*, 5.
[11] A. Rice, Y. Jin, X. F. Ma, X.- C. Zhang, D. Bliss, J. Larkin, M. Alexander, *Appl. Phys. Lett.* **1994**, *64*, 1324.
[12] Y.-R. Shen, *The Principles of Nonlinear Optics*, John Wiley & Sons Inc., New York **1984**.
[13] T. Seifert, S. Jaiswal, U. Martens, J. Hannegan, L. Braun, P. Maldonado, F. Freimuth, A. Kronenberg, J. Henrizi, I. Radu, E. Beaurepaire, Y. Mokrousov, P. M. Oppeneer, M. Jourdan, G. Jakob, D. Turchinovich, L. M. Hayden, M. Wolf, M. Münzenberg, M. Kläui, T. Kampfrath, *Nat. Photonics* **2016**, *10*, 483.
[14] D. Kong, X. Wu, Bo Wang, T. Nie, M. Xiao, C. Pandey, Y. Gao, L. Wen, W. Zhao, C. Ruan, J. Miao, Y. Li, Li Wang, *Adv. Opt. Mater.* **2019**, *7*, 1900487.
[15] Bo Wang, S. Shan, X. Wu, C. Wang, C. Pandey, T. Nie, W. Zhao, Y. Li, J. Miao, Li Wang, *Appl. Phys. Lett.* **2019**, *115*, 121104.
[16] A. Schneider, M. Neis, M. Stillhart, B. Ruiz, R U. A. Khan, P. Günter, *J. Opt. Soc. Am. B* **2006**, *23*, 1822.
[17] L. Wang, S. Kruk, K. Koshelev, I. Kravchenko, B. Luther-Davies, Y. Kivshar, *Nano Lett.*. **2018**, *18*, 3978.
[18] S. Liu, P P. Vabishchevich, A. Vaskin, J L. Reno, G A. Keeler, M B. Sinclair, I. Staude, I. Brener, *Nat. Commun.* **2018**, *9*, 2507.
[19] A E. Minovich, A E. Miroshnichenko, A Y. Bykov, T V. Murzina, D N. Neshev, Y S. Kivshar, *Laser Photonics Rev.* **2015**, *9*, 195.
[20] H. -. T. Chen, A. J. Taylor, N. Yu, *Rep. Prog. Phys.* **2016**, *79*, 076401.
[21] G. Li, S. Zhang, T. Zentgraf, *Nat. Rev. Mater.* **2017**, *2*, 17010.
[22] Z. Lin, L. Huang, Z. T. Xu, X. Li, T. Zentgraf, Y. Wang, *Adv. Opt. Mater.* **2019**, *7*, 21.
[23] S. Chen, F. Zeuner, M. Weismann, B. Reineke, G. Li, V. K. Valev, K. W. Cheah, N. C. Panoiu, T. Zentgraf, S. Zhang, *Adv. Mater.* **2016**, *28*, 2992.
[24] W.-Y. Tsai, T. L. Chung, H.-H. Hsiao, J.-W. Chen, R. J. Lin, *Adv. Mater.* **2019**, *31*, 1806479.

[25] S. Keren-Zur, M. Tal, S. Fleischer, D M. Mittleman, T. Ellenbogen, *Nat. Commun.* **2019**, *10*, 1778.
[26] M. Tal, S. Keren-Zur, T. Ellenbogen, *ACS Photonics* **2020**, *7*, 3286.
[27] E. Minerbi, S. Keren-Zur, T. Ellenbogen, *Nano Lett.* **2019**, *19*, 6072.
[28] L. Luo, I. Chatzakis, J. Wang, F B. P. Niesler, M. Wegener, T. Koschny, C M. Soukoulis, *Nat. Commun.* **2014**, *5*, 3055.
[29] C. Mcdonnell, J. Deng, S. Sideris, T. Ellenbogen, G. Li, *Nat. Commun.* **2021**, *12*, 30.
[30] J A. Schuller, E S. Barnard, W. Cai, Y. C. Jun, J S. White, M L. Brongersma, *Nat. Mater.* **2010**, *9*, 193.
[31] M W. Klein, C. Enkrich, M. Wegener, S. Linden, *Science* **2006**, *313*, 502.
[32] C. W. Hsu, Bo Zhen, A. D Stone, J D. Joannopoulos, M. Soljačić, *Nat. Rev. Mater.* **2016**, *1*, 16048.
[33] S I. Azzam, A V. Kildishev, *Adv. Opt. Mater.* **2020**, *9*, 2001469.
[34] A. Kodigala, T. Lepetit, Q. Gu, B. Bahari, Y. Fainman, B. Kanté, *Nature* **2017**, *541*, 196.
[35] M C. Gather, S. H. Yun, *Nat. Photonics* **2011**, *5*, 406.
[36] Z. Liu, Yi Xu, Ye Lin, J. Xiang, T. Feng, Q. Cao, J. Li, S. Lan, J. Liu, *Phys. Rev. Lett.* **2019**, *123*, 253901.
[37] Z. Yu, X. Xi, J. Ma, H Ki Tsang, C.-L. Zou, X. Sun, *Optica* **2019**, *6*, 1342.
[38] Z. Yu, Y. Tong, H Ki Tsang, X. Sun, *Nat. Commun.* **2020**, *11*, 2602.
[39] Y. Lu, Xi Feng, Q. Wang, X. Zhang, M. Fang, W. E. I. Sha, Z. Huang, Q. Xu, Li Niu, X. Chen, C. Ouyang, Y. Yang, X. Zhang, E. Plum, S. Zhang, J. Han, W. Zhang, *Nano Lett.*. **2021**, *21*, 7699.
[40] D. Sun, Y. Zhang, D. Wang, W. Song, X. Liu, J. Pang, D. Geng, Y. Sang, H. Liu, *Light: Sci. Appl.* **2020**, *9*, 197.
[41] Y. Jia, L. Wang, F. Chen, *Appl. Phys. Rev.* **2021**, *8*, 011307.
[42] P. C. Wu, C. Y. Liao, V. Savinov, T. L. Chung, W. T. Chen, Y.-W. Huang, P Ru Wu, Yi-H Chen, Ai-Q Liu, N I. Zheludev, D. P. Tsai, *ACS Nano* **2018**, *12*, 1920.
[43] V. G. Kravets, A. V. Kabashin, W. L. Barnes, A. N. Grigorenko, *Chem. Rev.* **2018**, *118*, 5912.
[44] P. Hoyer, M. Theuer, R. Beigang, E.-B. Kley, *Appl. Phys. Lett.* **2008**, *93*, 091106
[45] M. Wächter, C. Matheisen, M. Waldow, T. Wahlbrink, J. Bolten, M. Nagel, H. Kurz, *Appl. Phys. Lett.* **2010**, *97*, 161107
[46] K. Koshelev, S. Lepeshov, M. Liu, A. Bogdanov, Y. Kivshar, *Phys. Rev. Lett.* **2018**, *121*, 193903.